

Liquid Ferrofluid Synapses for Spike-based Neuromorphic Learning[†]

Charanraj Mohan, Marco Crepaldi, Diego Torraza, Andrew Adamatzky, Gisy Abdi, Aleksandra Szkudlarek, and Alessandro Chiolerio

Supplementary Information

S1 STDP and Biological Vs Neuromorphic vision systems

Spike Time Dependent Plasticity (STDP) is a group of spike-based bio-inspired computational neuroscience learning rules, which was first reported by Gerstner [1]. Later, the observation of such a rule in biological organisms was reported by many researchers [2, 3, 4, 5, 6, 7, 8, 9]. Consider a synaptic junction (characterized by synaptic weight) where the pre-synaptic and post-synaptic neurons connect as shown in Figure S1.

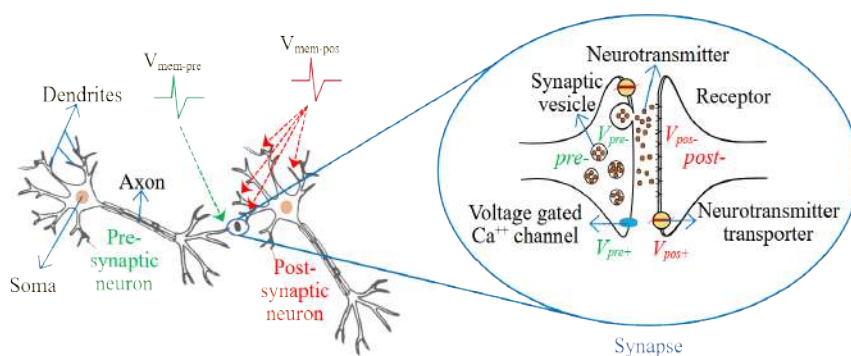


Figure S1: A synaptic junction that connects a pre-synaptic and post-synaptic neuron.

The pre-synaptic neuron sends an action potential- $V_{mem-pre}$ ($= V_{pre+} - V_{pre-}$) to the synapse, which cumulatively generates a post-synaptic action potential- $V_{mem-pos}$ ($= V_{pos+} - V_{pos-}$) at the membrane of the post-synaptic

neuron. Neurotransmitters are released into the synaptic cleft due to the pre-synaptic action potential. Each synapse or synaptic junction is characterized by synaptic weight (or strength)– w , which determines the efficacy of the pre-synaptic spike in contributing to the cumulative action at the post-synaptic neurons. According to the STDP, the change in synaptic weight, Δw is a function of the time difference between the pre-synaptic spike, t_{pre} and post-synaptic spike, t_{pos} . So, the change in synaptic weight, $\Delta w = \xi(\Delta T)$, where $\Delta T = t_{\text{pos}} - t_{\text{pre}}$. For positive ΔT a potentiation of synaptic weight happens i.e. $\Delta w > 0$ and for negative ΔT a depression of synaptic weight happens i.e. $\Delta w < 0$. Unlike Hebbian learning [10], which considers the mean firing rate of pre and post synaptic spikes, STDP takes into account the spikes' relative time. Figure S2 (a) shows the $N \times 1$ biological neurons interconnected by synapses whose simplified models are represented in Figure S2 (b). An example of silicon-morphed memristive circuit is shown in Figure S2 (c). Figure S2 (d) depicts the scheme of the human visual system, where the visual information is extracted through the retina, processed through the neurons, and finally recognized in the visual cortex. In analogy the neuromorphic vision system (as shown in Figure S2 (e)) identifies objects as events using an event-based camera whose information (in the form of spikes) is processed through I/O neurons and memristive crossbar.

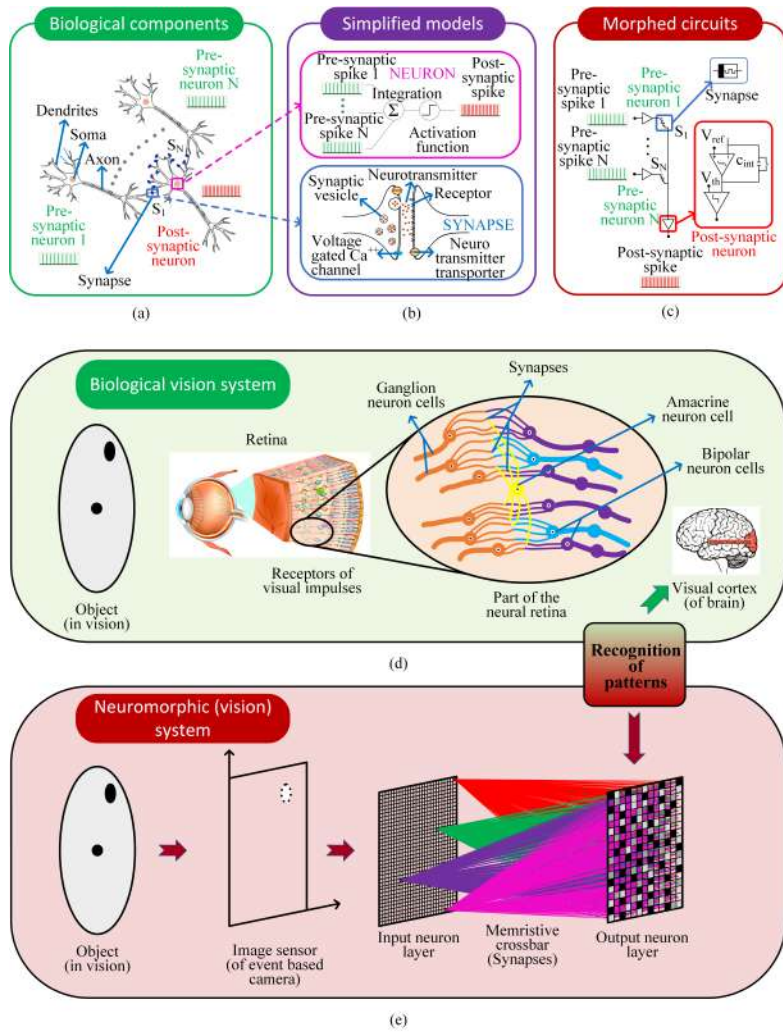


Figure S2: (a) Biological structure of neurons and synapses of an $N \times 1$ neural network, (b) Simplified models of a neuron and a synapse. Here, soma is modeled with a summation and activation function, (c) Morphed neuromorphic circuits of an $N \times 1$ neural network. Here, a leaky integrate and fire neuron is considered as a post-synaptic neuron, and memristors as synapses, (d) Scheme of the biological visual system (Retina- ©sakurra/stock.adobe.com, Visual cortex- ©2008 Centre of Excellence for Early Childhood Development, Encyclopedia on Early Childhood Development, Glossary-Brain, December 3, 2008.), (e) Scheme of the neuromorphic (vision) system.

S2 Reliability issues with solid state memories

Though solid-state memories are the prominent candidates for monolithic integration with Complementary Metal Oxide Semiconductors (CMOS) technologies they face severe reliability issues. Some notable reliability issues are– the ‘write’ failure in complementary switching of bipolar Resistive Random Access Memory (RRAM) [11], the endurance failure in RRAM due to anode oxidation induced interface reaction, the ‘erase’ failure effect attributed to extra vacancy and depletion of O^{2-} induced R_{HRS} reduction [12], the ‘erase’ failure in RRAMs due to overgrowth of metal filament into the inert electrode and formation of a cation source [13, 14, 15], the spurious change of the state of Spin Transfer Torque Magnetic Random Access Memories (STT-MRAMs) by read currents due to their limited thermal stability [16], the occurrence of oxide barrier breakdown and shortening of the lifetime of Magnetic Tunnel Junction (MTJ) when switching the STT-MRAMs faster [17], the reduced Tunnel Magneto Resistance (TMR) ratio under bias voltage when using an ultra-thin oxide barrier for low resistance area product in STT-MRAMs [18], the delamination [19] and occurrence of other mechanical failures (such as cracks, local material stoichiometric changes, material interdiffusion, etc.) [20] in Phase Change Memories (PCMs) when the ‘erase’ pulse is applied for few ns after reaching the melting temperature, the unintentional heating of PCM layer induced by thermal cross-talk between adjacent bits [21], the reduced ‘write’ time results in elevated temperature instabilities [22], the resistance drift and decay in the ‘write’ state [23] in PCMs, the endurance failure in HfO_2 - based Conductive Bridge Random Access Memories (CBRAMs) due to copper accumulation in filament [24], the programming failure due to negative-‘write’ behaviour [25] and reduced off-state resistance due to over-injection of cations into electrolyte layer [26, 27] in CBRAMs, fatigue failure [28, 29, 30] and imprint failure [31] in Ferroelectric Random Access Memories (FeRAMs).

Most solid state memories are also sensitive to statics and are prone to mechanical (at the microscopic levels) damages due to electrostatic discharge (ESD) unless they are monolithically integrated to silicon and are protected by clamped diodes. The static sensitive CBRAM suffer from irreversible damaged by ESD [32]. CBRAMs also get damaged by the high open-circuit voltage when measured by a multi-meter [32]. MTJs exhibit degradation characteristics as a result of increased ESD levels thereby resulting in MTJ instability [33], whereas ESD events trigger resetting PCMs [34]. Moreover, it is quite feasible that the states of the memristors changes when the ESD protection circuits are not properly deployed [35].

S3 Physico-chemical characterization of ferrofluids

Scanning Electron Microscope (SEM) analyses are performed using sample drop casting on silicon wafers. After the evaporation of the solvent under vacuum,

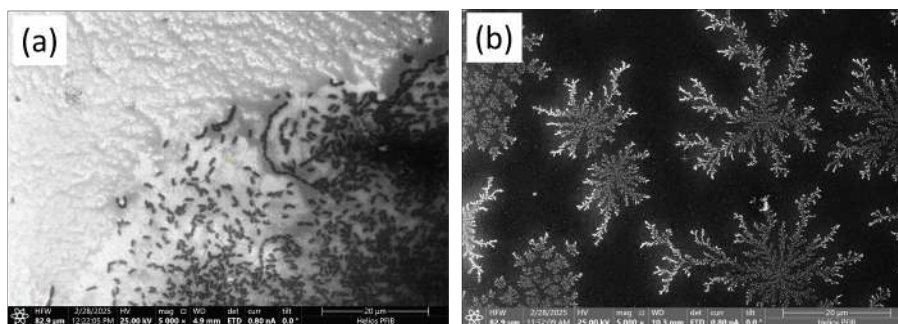


Figure S3: Morphological inhomogeneities of dried nanoparticles seen at SEM: (a) PL sample showing chain-like arrangements of nanoparticles, (b) EMG sample showing fractal arrangements of nanoparticles.

sample PL (or PL-M-Fe₃O₄) [36] presented some chain-like clustering and sample EMG (or EMG 601p) [37] showed crystalline remnants around the nanoparticles (see Figure S3). Energy Dispersive X-ray (EDX) spectra after drop-casting on a Si wafer, normalized with respect to the signal from Si, are shown in Figure S4. Selected Area Electron Diffraction (SAED) patterns of the two samples are shown in Figure S5, together with the ring identification and crystal structure tables. High Resolution Transmission Electron Microscopy (HRTEM) images of the two samples are shown in Figure S6 and X-ray Photoelectron Spectroscopy (XPS) survey spectra for the two samples are shown in Figure S7.

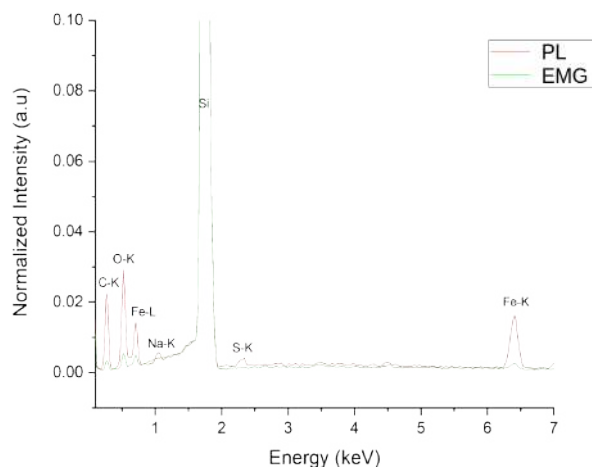


Figure S4: EDX spectra of the two dried samples.

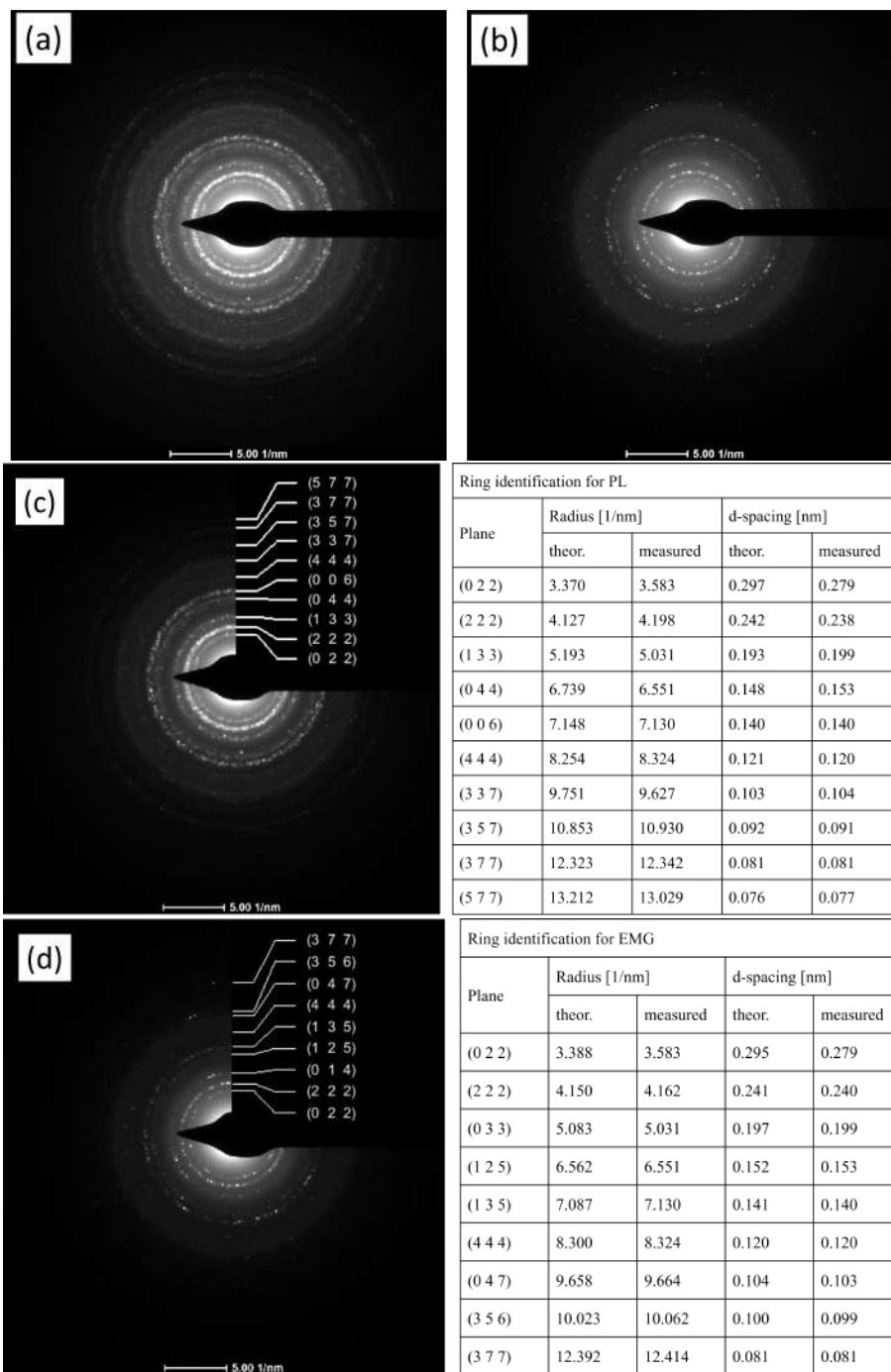


Figure S5: SAED patterns of the two samples: (a) PL sample, (b) EMG sample, Ring analysis of the two samples: (c) PL sample, (d) EMG sample.

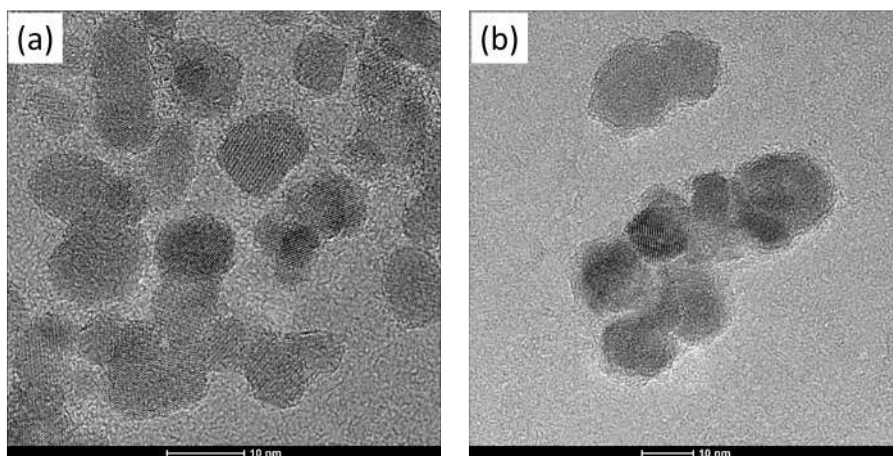


Figure S6: High Resolution TEM images of the two samples: (a) PL sample, (b) EMG sample.

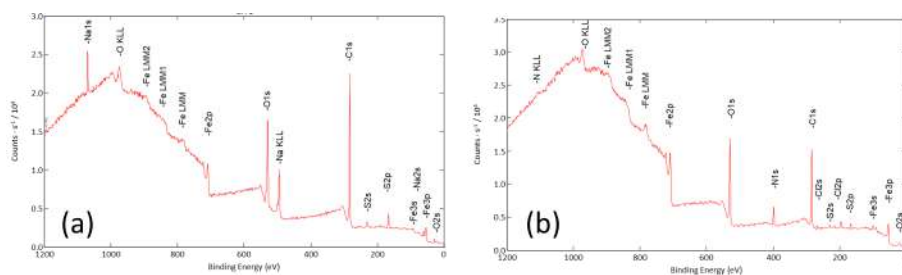


Figure S7: XPS Survey spectra of the two samples: (a) PL sample, (b) EMG sample.

S4 Design of the vials

Two vials are designed to contain the ferrofluid and characterize its states. One vial is designed for a fixed volume of about 6 cc (maximum) and another with an adjustable volume (in the range 0.174 cc to 15.11 cc) and an adjustable electrodes' distance. Both the vials are Computer Numerical Control (CNC) machined- using Polytetrafluoroethylene (PTFE)- a teflon material for containing the ferrofluid and using AA-7075 Aluminium alloy as the outer shield. Teflon is used as inner chambers to contain the ferrofluid due to its excellent chemical and temperature resistance properties. Moreover, its non-sticky and low frictional properties are very suitable to handle the ferrofluid. AA-7075 is chosen for designing the outer shielding due to its higher strength, low density, better corrosion resistance, and easy CNC machining. Two electrodes of the SMA (Sub-Miniature version A) connector are submerged inside the ferrofluid by which the

electrical stimuli are applied. There are seals rings (O-rings) on the electrodes, and on upper lid of the inner cylinder and this makes the ferrofluid completely sealed from the outer environment. There are also seal rings on the pistons, connection block, and valves in the vial with adjustable volume. The seal rings are made of Nitrile Butadiene Rubber (NBR) polymer.

S4.1 Vial with fixed volume

This vial is designed to have a fixed volume of maximum of 6 cc depending on the quantity of the ferrofluid poured into the vial. It is also designed with a fixed distance of 10 mm between the electrodes. Modification in volume can not be done real-time when the experiments are going on. Instead the only way to change the volume is to add or remove ferrofluid by unscrewing the top metal plate, and opening the teflon lid. The vial has a total height of 80.5 mm and area of the square shaped based is about 250 mm². The bisected and the lateral view of the vial with fixed volume along with its dimensions and internal parts duly labelled is illustrated in Figure S8. The diameter of the inner cylinder is 10.8 mm and its height is 54 mm excluding the inverted cone shaped bottom part. The part of the electrodes of the SMA connectors submerged into ferrofluid is about 0.9 mm.

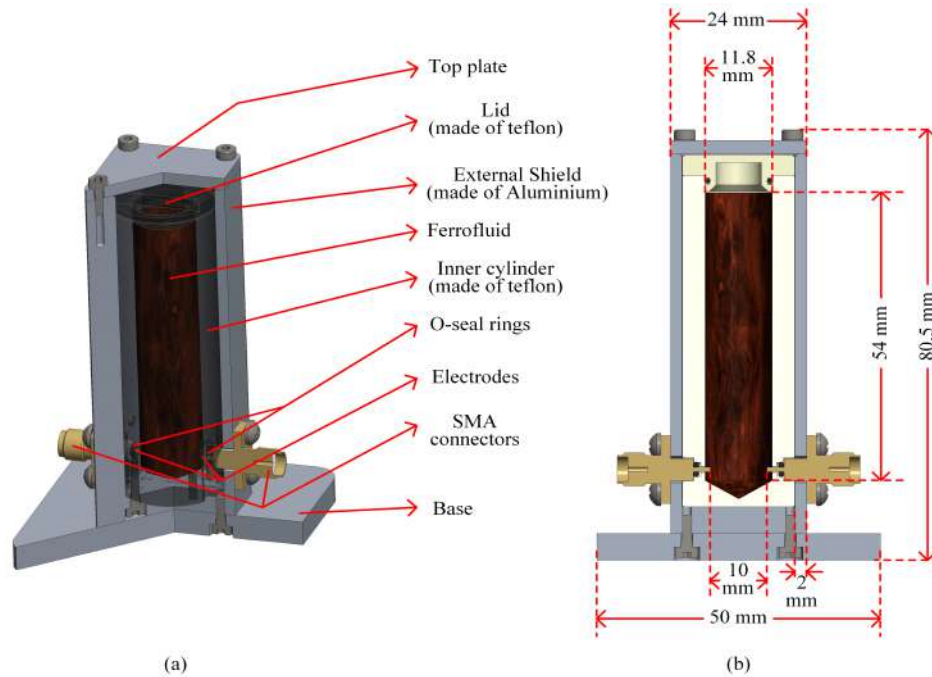


Figure S8: Different views of the vial with fixed volume: (a) Bisected view of the vial, (b) Lateral view of the vial

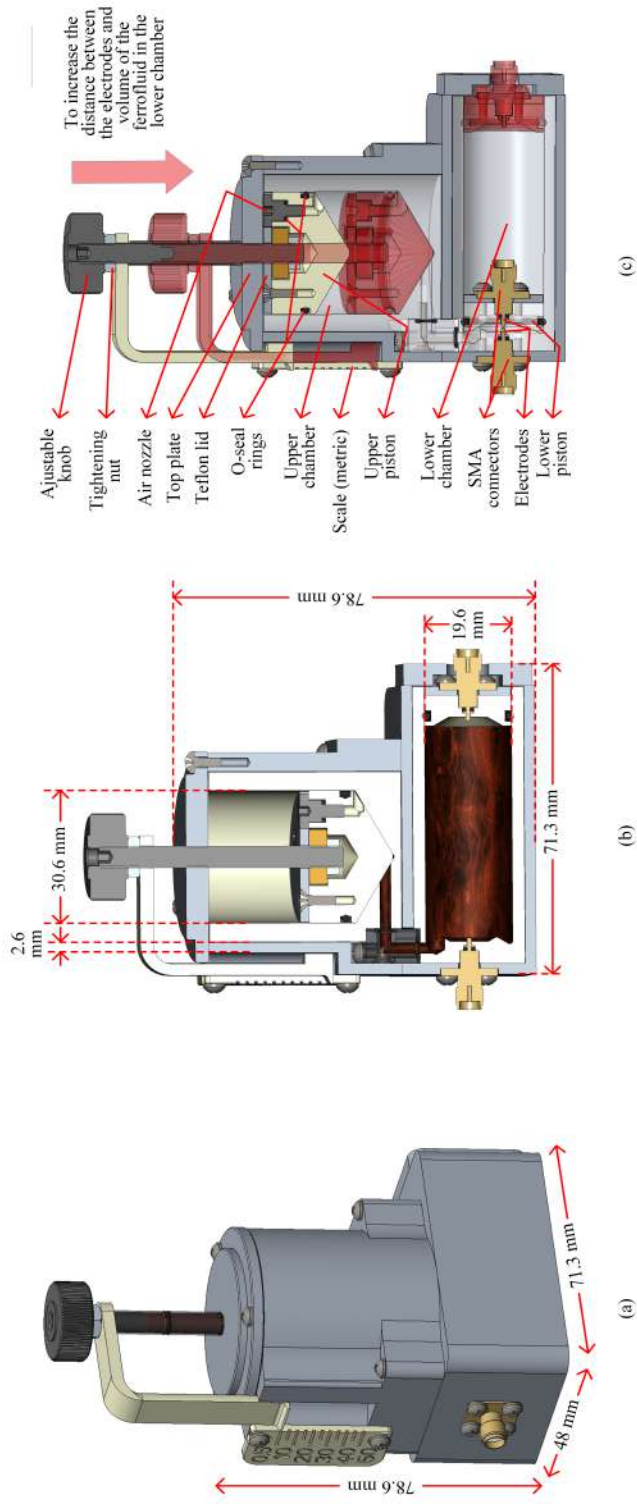


Figure S9: Different views of the vial with adjustable volume: (a) 3D view of the vial, (b) Lateral view of the vial, (c) Lateral view of the vial where the positions of maximum and minimum distance between the electrodes are highlighted.

S4.2 Vial with adjustable volume

This vial facilitates adjusting the distance between the electrodes without the necessity to open the top plate and inner teflon lid. Figure S9 shows the 3D and lateral view of the vial with dimensions and internal parts duly labelled. This is implemented by designing a piston system that is moved manually to pump in and pump out the ferrofluid between the upper and lower chambers. The upper chamber serves as a reservoir for ferrofluid, while the lower chamber is used to contain and characterize the ferrofluid via the SMA connectors. One of the SMA connectors is fixed while the other is movable. The movable SMA connector is coupled to the piston which moves with the incoming ferrofluidic pressure. There is a handy adjustable knob at the top of the vial by which the piston of the upper chamber is moved in both upward and downward directions which in turn pumps out and pumps in the ferrofluid at the lower chamber. An air nozzle is designed at the top of the upper chamber to vent out any air bubbles when filling the ferrofluid in it. A metric scale is designed whose level-indicating gauge is suspended from the top screw of the vial. The gauge is kept in the correct position by two springs (not shown in Figure S9) that enables pushing up against the tightening nut that is below the adjustable knob. The metric scale guarantees the correct indication of electrodes' distance.

The designed vial's volume is determined by the expression,

$$V = 174 + \pi * R^2 * (L - 0.5) \text{ mm}^3 \quad (1)$$

where L is the distance between the electrodes in mm and R (= 9.8 mm) is the radius of the lower chamber. 174 mm^3 is the minimum volume of the ferrofluid when the electrodes are at the shortest possible distance of 0.5 mm. The vial design also attributes an additional 2% of the minimum volume for every pair of seal rings due to the gaps between the metal and the wrapped seal ring.

S5 Characterization experiments

Unlike most solid-state devices, the ferrofluid's Low Resistance State (LRS) slowly settles to the High Resistance State (HRS) due to its Short Term Plasticity (STP). Therefore the post-write resistance state has a short lifetime, and it must be read before the liquid synapse navigates towards HRS. Figure S10 shows the analog and digital signals applied during characterization. During the read time (t_r), a particular sample is targeted and recorded uniformly during read after every write and erase operation, where the applied read biases are positive values. The samples are highlighted in the Figure. S10 (c), where samples- S_{w3} and S_{e3} are targeted. This sample is chosen as there is a visible LRS value and where the STP starts to ease. Figure. S13 shows the resistance, R_{AB} of the ferrofluid (stabilized by oleic acid) when DC sweeps are carried out for 30 full-cycles of switching between the Erase and Write cycles. The IV characteristics of the corresponding DC sweeps are shown in Figure. 6 (c) of the main manuscript.

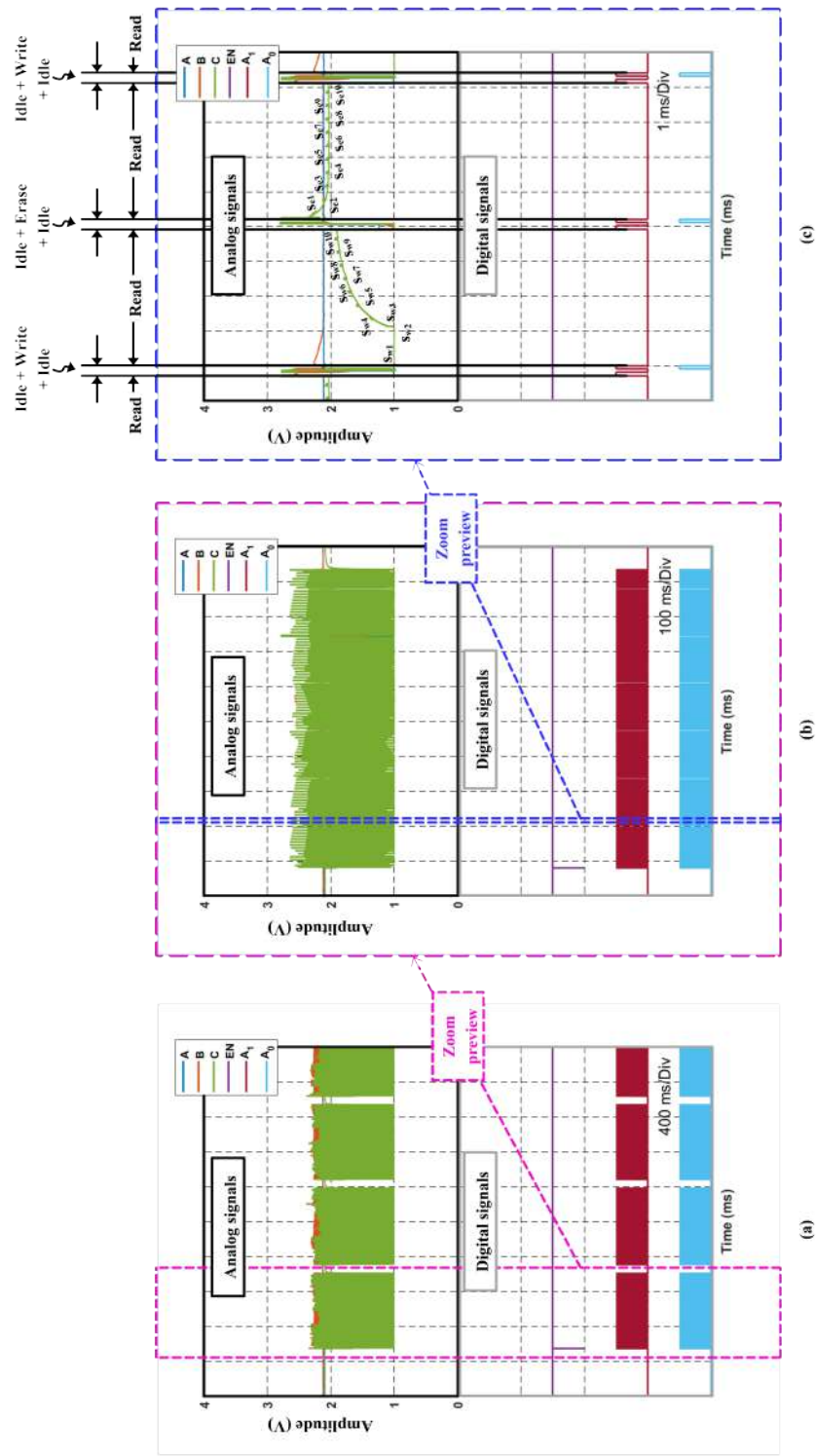


Figure S10: Analog (A, B and C) and digital signals (EN, A₀, A₁) during characterization: (a) Trains of characterization pulses applied across the vial, (b) Zoom preview of 100 characterization pulses applied across the vial, (c) Ultra-zoom preview of a pair of switching pulses (write followed by read and erase followed by read) applied across the vial.

Table S1: Bias conditions for resistance switching in pulse mode

Parameters	Values
Read time, t_r	2 ms
Erase time, t_e	11 μ s
Write time, t_w	11 μ s
Read bias, v_r	14 mV
Erase bias, v_e	- 0.24 V
Write bias, v_w	1.53 V
Threshold post-erase resistance, r_e	15 k Ω
Threshold post-write resistance, r_w	600 Ω
Feedback resistance, r_f	20 k Ω

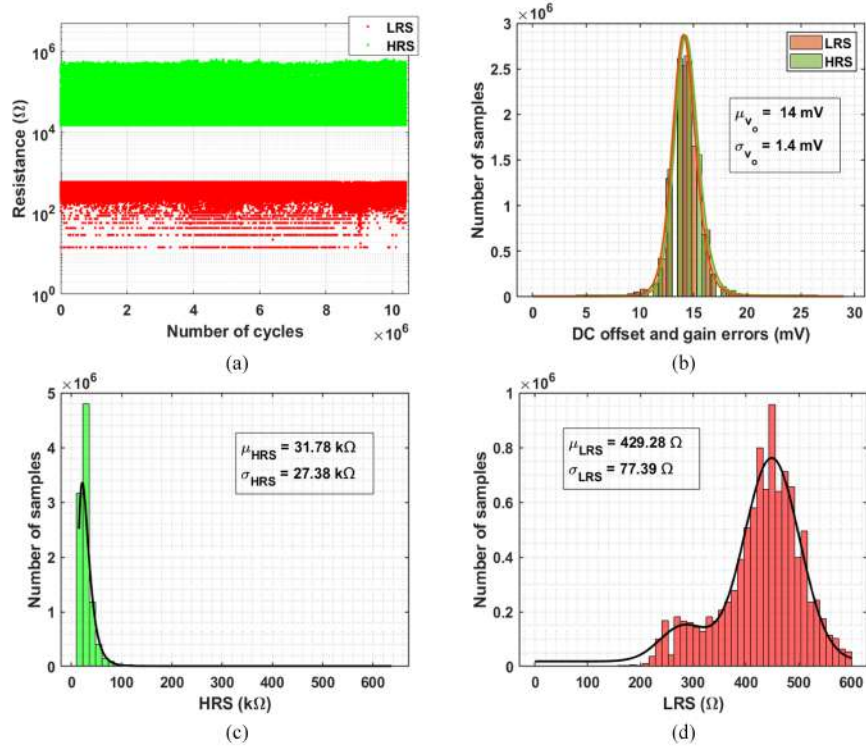


Figure S11: Results of the resistance switching in ferrofluid (with water-soluble dispersant) using dynamic pulse mode for 10 Million endurance cycles: (a) HRS and LRS values, (b) Statistical spread of the applied read voltage, v_r , (c) Statistical spread of the HRS values, (d) Statistical spread of the LRS values.

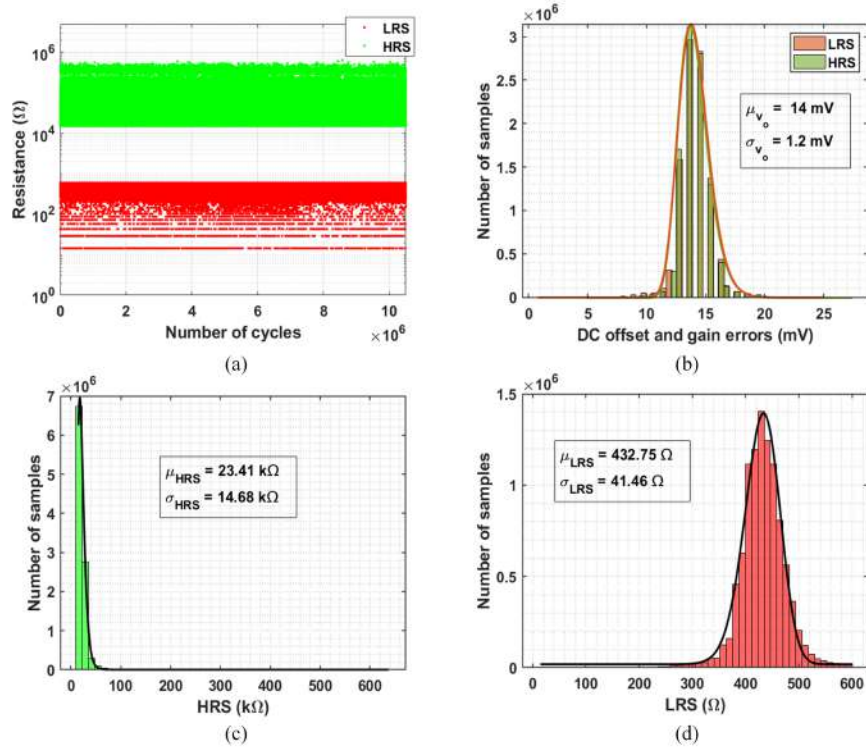


Figure S12: Results of the resistance switching in ferrofluid (30 % conc. ca. oleic acid) using dynamic pulse mode for 10 Million endurance cycles: (a) HRS and LRS values, (b) Statistical spread of the applied read voltage, v_r , (c) Statistical spread of the HRS values, (d) Statistical spread of the LRS values.

Table S2: Bias conditions for the DC sweep experiment

Parameters	Values
Number of cycles, cycle	30
Read time, t_r	2 ms
Erase time, t_e	66.6 μ s
Write time, t_w	20 μ s
Sweep voltage for erase, v_{s_e}	0.75 V
Sweep voltage for write, v_{s_w}	1.9 V
Read bias, v_r	0.32 V
Step voltage of the DAC, v_s	12.89 mV
Threshold post-erase resistance, r_e	35.5 k Ω
Threshold post-write resistance, r_w	7 k Ω
Feedback resistance, r_f	20 k Ω
Set voltage (observed), v_{set}	0.2 V
Reset voltage (observed), v_{reset}	-0.16 V

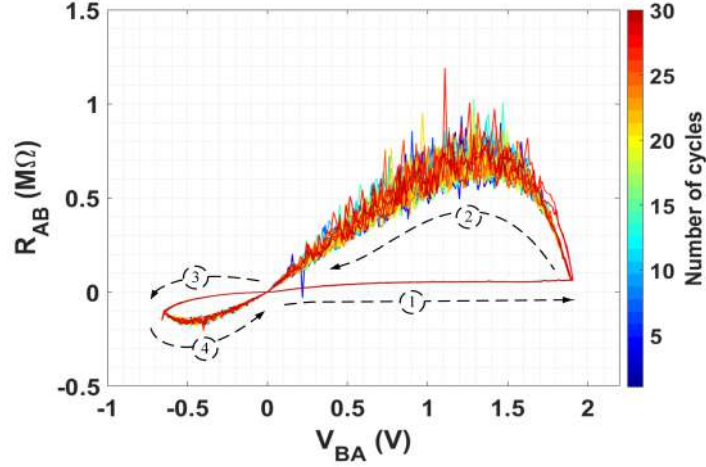


Figure S13: Resistance Vs DC sweep voltage plot of the ferrofluid (stabilized by oleic acid) for 30 full-cycles of switching between the Erase and Write cycles.

Figure. S11 and Figure. S12 shows the endurance characterization results (HRS and LRS values, statistical distribution of the resistance values and the read voltages) in dynamic pulse for 10 Million cycles for both ferrofluid with water-soluble dispersant and ferrofluid stabilized by oleic acid. Due to the stability of suspended nanoparticles in the latter variations of the HRS and LRS values are reduced by 46 %. Table S2 and Table S1 show the bias conditions for DC sweep and resistance switching in pulse mode experiments respectively. For resistance switching in pulse mode, an additional check to verify the positive magnitude read pulse is implemented as read pulses of less magnitude are applied.

S6 LTP characterization of ferrofluids

Long Term Plasticity (LTP) measurements are performed using a Semiconductor Characterization System 4200-SCS from Keithley - Tektronix, equipped with two independent Pulse Measurement Units (PMUs), connected to the fixed volume vial hosting 2 mL of ferrofluids at room temperature. Measurements are carried out by applying a positive (or negative) pulse lasting for 1 ms with a 50 % duty cycle, and with an amplitude of +/-10 mV, with rise and fall times equal to 1 μ s. The pulse is applied 1, 10, 100, 1000 and 10.000 times while collecting and averaging data, recording both current and voltages on both of the PMUs. The resulting true resistance of the ferrofluids (both PL and EMG) is shown in Figure S14, where LTP effects are realized even with input biases of lower magnitude (+/-10 mV). The main observations are: PL has initially a resistance of 1035 Ω (or 0.9662 mS of conductance), while the effects of LTP after applying 10^3 positive pulses produce a final resistance state of 2635 Ω (or

0.3795 mS of conductance). EMG has initially a resistance of 1185 Ω (or 0.8439 mS of conductance), while the effects of LTP after applying 10^3 positive pulses produce a final resistance state of 2235 Ω (or 0.4474 mS of conductance). These results demonstrate a depression of 60.72 % and 47 % of the PL and EMG ferrofluids respectively due to the LTP effects. On the contrary, when negative pulses are applied, the potentiation is less effective yet measurable (see Figure S14 (c) and (d)). When we consider the initial state the resistance after 10^2 pulses, including the settling time and the behaviour reversal, PL ferrofluid has an initial resistance of 2606 Ω (or 0.3837 mS of conductance) and a final state of 2173 Ω (or 0.4602 mS of conductance), after applying 10^3 negative pulses. Similarly, the EMG ferrofluid has an initial resistance of 1909 Ω (or 0.5238 mS of conductance) and a final state of 1865 Ω (or 0.5362 mS of conductance). These results obtain a potentiation of 20 % and 2.4 % of the PL and EMG ferrofluids respectively due to the LTP outcome. Figure S14 also signifies enhanced LTP programmability features of PL ferrofluid when compared to its counterpart EMG even for the applied lower amplitude of 10 mV.

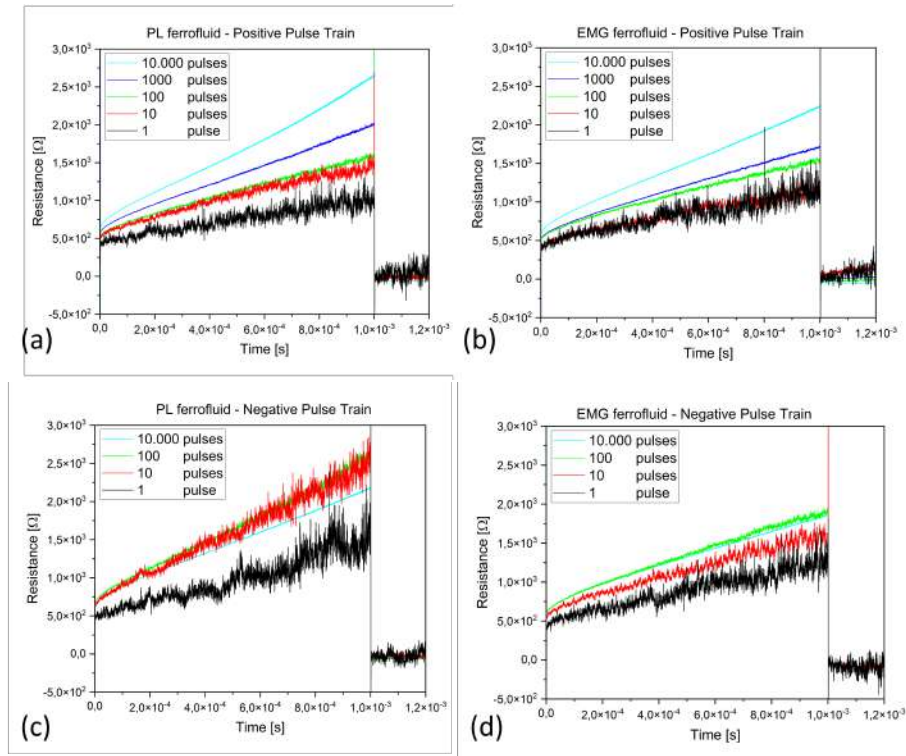


Figure S14: LTP pulse train characterization: (a) PL sample potentiation, (b) EMG sample potentiation, (c) PL sample depression, (d) EMG sample depression.

S7 Comparison of Ferrofluid with other memory technologies and experiments on scalability feature of the ferrofluidic synapse

Table S3 lists the comparison of materials, dynamic range, ON/OFF ratio, switching speed, area/volume, relative cost, power (both during programming and read), read bias, endurance cycles, volatility nature, stochastic nature, and characterization platform of ferrofluid with the different memory technologies. A comparison of both ON/OFF ratio and read bias of our work with others where the applied read voltage is less than 100 mV is shown in Figure. S15 [47, 48, 49, 50, 51, 52, 53, 54, 55, 56].

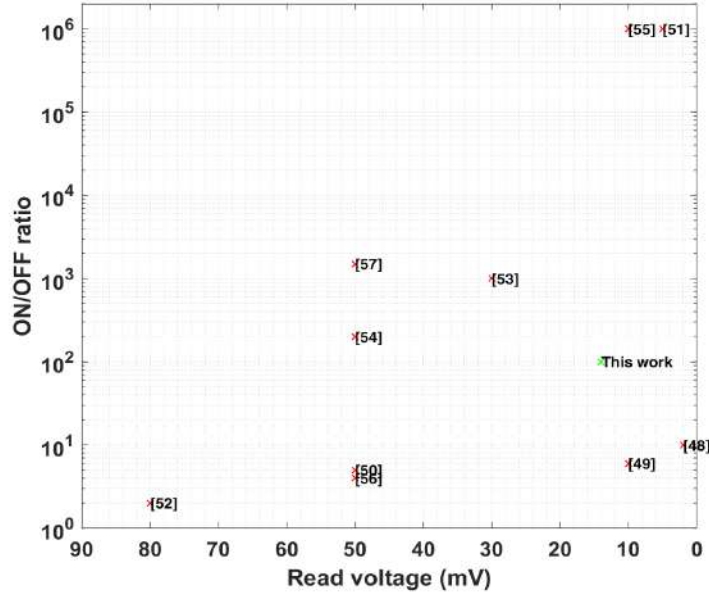


Figure S15: Comparison of both ON/OFF ratio and read bias of our work with others, particularly when the applied read bias is less than 100 mV.

To validate the functionality of the ferrofluid by scaling down both the volume (V) of the ferrofluid and the distance between the electrodes (L), we designed the vial with adjustable volume as explained in Section 4.2, and conducted characterization experiments. By the relation in Equation 1, the distance between the electrodes is varied in the range ($500 \mu\text{m} \leq L \leq 50 \text{ mm}$) to have their corresponding volume of the ferrofluid. Experiments of 10^4 characterization resistance switching cycles are conducted and their average values for different mean read voltages (14.1 mV, 27.1 mV, 39.6 mV and 52.9 mV) are determined for various distances between the electrodes. These results are shown in Figure.

Table S3: Comparison of liquid-based magnetite with existing major memory technology categories

Device (Composition)	Cu-MgO-CoFeB-BEC ^b -Cu[40]	TiN-Pt-(15 alt. layers of GST467 ^c -TiTe ₂)-TiN[41]	TiN-Si:HfO-Ti -TiN[42]	Ag-WTe ₂ -Pt[38]	TiN-HZO ^a -TiN[39]	Fe ₃ O ₄ (This work)
Category	STT-MRAM	PCM	ReRAM	CBRAM	FERAM	Magnetic NPs
Type	Solid state	Solid state	Solid state	Solid state	Solid state	Liquid
Dynamic range (V)	-1.5 to 1.5	-0.7 to 0.7	-3 to 3	-0.8 to 1.35	-2.5 to 2.5	-0.65 to 1.9
ON/OFF ratio	2	$\sim 10^2$	~ 10	$> 10^3$	10^3	$> 10^2$
Switching speed	90 ns	40 ns	1 μ s	200 ns	10 ns	20 μ s
Area/Volume	0.933 μ m ²	-	100 μ m ²	-	0.06 μ m ²	174 μ L
Cost ^d	High	High	High	Medium	High	Low
Power (Prog.)	150 μ W	60 μ W	-	in mW regime	-	-
Power (read) ^e	-	0.25 μ W	5.3 nW	0.4 mW	-	30 μ W
Read bias (V)	-	50 m	400 m	150 m	100m	≥ 14 m
Endurance (cycles)	$> 10^{10}$	2×10^8	$> 10^8$	$> 2 \times 10^7$	$> 10^9$	$> 10^7$ ^f
CMOS integration ^g	28 nm tech.	Compatible	130 nm tech.	no	60 nm tech.	feasible ^h
Add. bias/constraints	TDC ⁱ readout	Resistance drift ^j	Extra forming ^k	High switching currents ^l	-	-
Volatile nature	Non-volatile	Non-volatile	Non-volatile	Non-volatile	Non-volatile	Volatile
Intrinsic stochasticity	Unavoidable[43]	Unavoidable[44]	Unavoidable[45]	Unavoidable[46]	-	Absent
Charact. platform	MCU ^m on an evaluation board via a SPI ^o	On wafer measurements	SDPA ⁿ , waveform generator SMUs ^p	parameter analyzer	On wafer measurements	Custom-made PCB, and driver board

^aHf_{0.5}Zr_{0.5}O₂
^bBottom Electrode Contact.

^cGe₄Sb₆Te₇
^dRelative cost of memory without CMOS integration.

^ePower when reading an LRS value is considered whose read current is high.

^fAdding a couple of decades of characterization results take about 200 days and hence we have stopped characterizing until 10^7 cycles. In principle, the ferrofluid exhibit an unlimited endurance due to its amorphous nature.

^gBEOL (Back End Of Line)- described in Section 8 (1) of the Supplementary material.

^hDue to the low dynamic range of switching, possible integration with ≤ 28 nm CMOS technologies is feasible.

ⁱTime-to-Digital Converter (TDC) read out limits crossbar array size.

^jGradual change of resistance over time is resistance drift. GST467 suffers low resistance drift compared to GST225 (Ge₂Sb₂Te₅).

^kForming is the procedure to bring the device from Pristine Resistive State (PRS) to Low Resistive State (LRS).

^lHigh switching currents needs a large current-limiting transistor and this severely limits scalability.

^mMicro Controller Unit.

ⁿSemiconductor Device Parameter Analyzer

^oSerial Peripheral Interface.

^pSource Measure Units.

S16, where each plotted value is an average value of 10^4 resistance switching characterization cycles. The prime observation is the exponential increase in electric field when we minimize the distance between the electrodes, thereby keeping healthy yield and ON/OFF ratio. The yield is mainly affected by two factors, as explained in Section 4 of the main manuscript and the average yield obtained in these experiments is about 97 %. There is about a decade increase in electric field when the distance between the electrodes (L) is minimized from 5.25 mm to 500 μm . On further minimizing L to 50 nm (by the factor 10^4), the electric field can approach in the range of 10^6 N/C, similar to the electric field ranges of solid state memories (For example- OxRAM's electric field is about 2.2×10^6 N/C [57], STT-MRAM's electric field is 0.83×10^6 N/C [58]). These experiments clearly indicate the possible capability of scaling down the size of the ferrofluid synaptic devices like solid state memories.

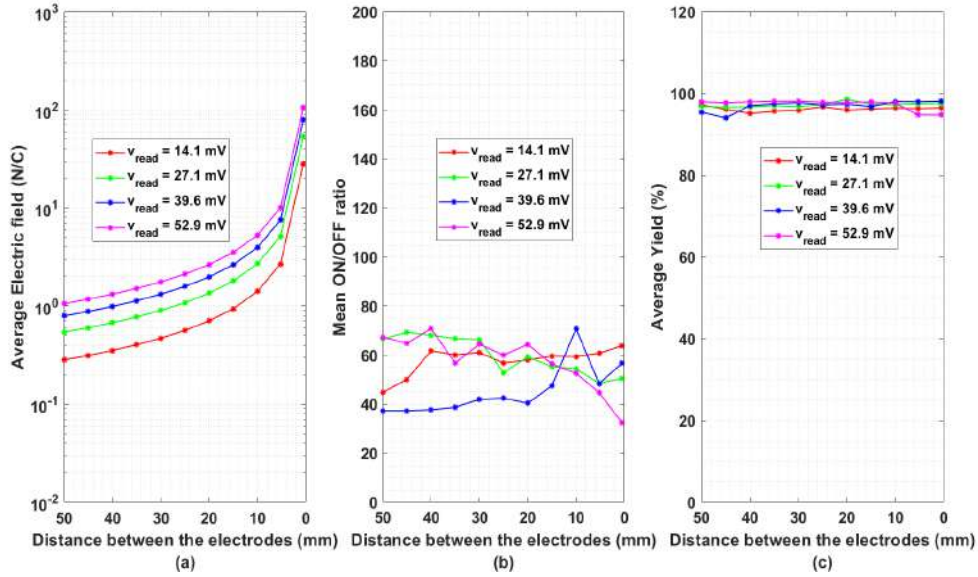


Figure S16: Experimental results for 10^4 characterization cycles: (a) Comparison of average Electric field for different read voltages, (b) Comparison of mean ON/OFF ratio for different read voltages, (c) Comparison of average yield for different read voltages.

S8 Learning patterns by Unsupervised STDP learning rule

Table S4: Bias conditions and values of the components for pre-synaptic drivers, post-synaptic neurons, and the controls for the switches (near synapses) in the 4×4 synaptic crossbar

Parameters	Values
Top terminal read active bias, V_{tra}	0.9153 V
Bottom terminal read active bias, V_{bra}	0.9 V
Top terminal read default bias, V_{trd}	0.9 V
Bottom terminal read default bias, V_{brd}	0 V
Top terminal write active bias, V_{twa}	1.53 V
Bottom terminal write active bias, V_{bwa}	0 V
Top terminal write default bias, V_{twd}	0 V
Bottom terminal write default bias, V_{bwd}	0 V
Top terminal erase active bias, V_{tea}	0 V
Bottom terminal erase active bias, V_{bea}	0.24 V
Top terminal erase default bias, V_{ted}	0.24 V
Bottom terminal erase default bias, V_{bed}	0 V
Top terminal idle active bias, V_{tea}	0 V
Bottom terminal idle active bias, V_{bea}	0 V
Top terminal idle default bias, V_{ted}	0 V
Bottom terminal idle default bias, V_{bed}	0 V
Top terminal reset bias, V_{treset}	0 V
Bottom terminal reset bias, V_{breset}	0 V
Erase time, t_e	11 μ s
Write time, t_w	11 μ s
Integrating capacitor, c_{int}	25 nF
Reference voltage for comparator, v_c	0.82 V

Table S4 lists the values of the biases and passive components used in the pre-synaptic drivers, post-synaptic neurons, and the controls for the switches (near synapses). Figure. S17 (a) shows how the initial (randomly considered) weight, W_{ini} evolves to the learned weights, W_4 with four STDP weight updates. The patterns considered for learning are applied in the form of read pulses of magnitude 15.3 mV across the rows of the synaptic crossbar and are illustrated in Figure S17 (b). The mean read bias of the first 10^4 characterization cycles of the ferrofluid (as shown in the Figure. S11 (d)) is 15.3 mV. Although the neurons learn in a few epochs of weight update, this means that the read voltage is applied considering the scalability of larger crossbars. The patterns are applied in batches across the rows of the crossbar as illustrated in Figure. S17 (c) and a cycle comprises applying all unique patterns (Pattern 1, Pattern 2, Pattern

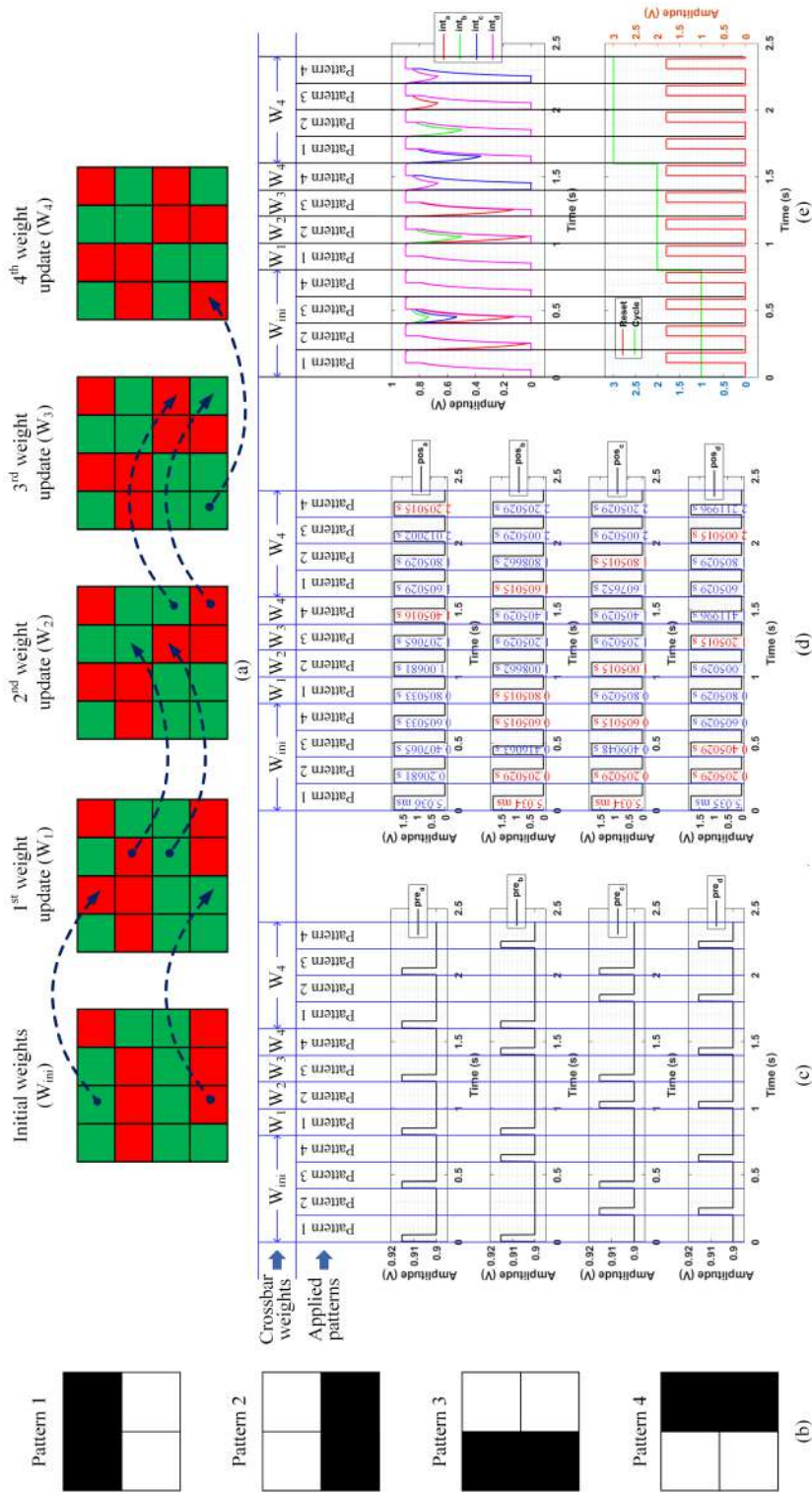


Figure S17: (a) STDP weight updates carried out in steps in the 4×4 synaptic crossbar, (b) Patterns in the 4×4 pixel considered for learning, (c) Patterns applied across the crossbar in the form of read pulses of magnitude, 15.3 mV, (d) Outputs waveforms of the post-synaptic neurons with labeled spiking times, (e) Reset and number of cycles (of the post-synaptic neurons).

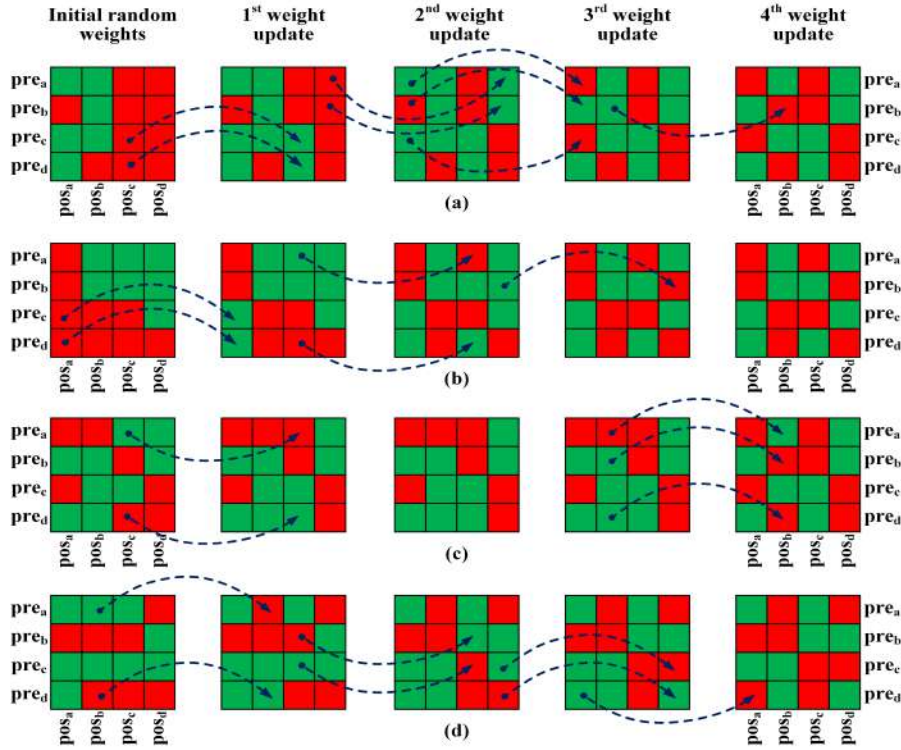


Figure S18: STDP weight updates (step-by-step) for four different random initial weights.

3, and Pattern 4) for learning once. The time for feeding each pattern (along with the ‘reset’ signal) to the system is about 0.2 seconds. The ‘reset’ is carried out for the post-synaptic neurons at the end of each pattern. Hence, for a single inference i.e. applying all the patterns once is done in 0.8 s time. There are two inferences (without any weight update) carried out to see the response of the neurons without learning and with learning the patterns. One at the beginning between 0 and 0.8 s and one at the end between 1.6 s and 2.4 s. The one at the end is similar to template matching, which is applying a single inference of input patterns on the learned weights. The STDP weight updates are carried out between 0.8 s and 1.6 s. The post-synaptic outputs along with their labeled spiking times are illustrated in Figure. S17 (d), where the spiking time of the neuron(s) that fire early for each input pattern is/are highlighted in ‘red’ color. Indication in the ‘red’ color is done to visualize how the neurons learn as time evolves with the STDP weight update on the synaptic crossbar. In this learning process, if a neuron spikes earlier for a particular input of pattern, it infers- the particular neuron for learning the pattern. The time difference between the fastest neuron and the second fastest one is incidentally kept as

14 μs in order to accommodate the learning process below or within a few μs range due to the ferrofluid's short-term plasticity. During the first inference (i.e. during W_{ini}), we can see that more than two neurons spike faster and at the same time. When the STDP weight updates are carried out we can observe how each neuron learns a particular pattern after learning during W_4 . For example- during weight update, W_1 post-synaptic neuron, pos_b learns pattern 1. Likewise, after three weight updates, each unique post-synaptic neuron is capable of firing early, thereby learning each pattern distinctly. Figure. S17 (e) shows the integrators' output waveform of the post-synaptic neurons and the reset and the number of cycles. The integrated outputs are compared with the reference voltage, v_c , and digital outputs are generated at the post-synaptic neurons. Figure. S18 shows the step-by-step STDP weight updates for four different initial weights. As different initial weights are considered, the neurons learn differently in these cases. For example- In Figure S18 (a), post-synaptic neuron, pos_a learns Pattern 3, while in Figure S18 (b) the same neuron learns for Pattern 1.

S9 Terminologies, phrases and additional clarifications

1. **Back End Of Line (BEOL)**- is the final state of semiconductor processing that concerns the interconnects, residing in the top part of a chip, which is offered by a few foundries [59, 60]
2. **NEEL temperature**- is the temperature above which certain antiferromagnetic materials become paramagnetic. At ~ 850 K magnetite (Fe_3O_4) undergoes a transition to a paramagnetic state.
3. **Step voltage of the micropython board**- is the finest output voltage of the MicroPython board's DAC. As we have an 8-bit DAC, $v_{\text{step}} = 12.89$ mV, excluding the gain and offset errors.
4. **Restricting the measurements to 10 Million endurance cycles**- It takes about 2 full days to characterize and collect 10 Million endurance cycles' results using our proposed system. This is mainly due to the speed of the ADCs in the MicroPython board and the communication protocol with the host computer, as it certainly involves- displaying all desirable data values in the terminal window through which the MicroPython board is connected to the computer and then exporting them to a .csv file at the end of the experiment. As an estimate, repeating the experiment of resistance switching in dynamic pulse mode for 1 Billion cycles would take about 200 days. Due to the requirement of the large time frame, we have stopped characterizing until 10 Million cycles. Moreover, the controllable resistance switching and the fault-tolerant capability of the colloid enables an everlasting resistance switching without any failure; unlike solid-state memories.

5. **Fitting curves of the distribution-** The fitting curves used in the statistical spreads of all the figures in the main manuscript and the supplementary material are either implemented using Pearson IV lognormal or multiple gaussian distribution fitting techniques.

References

- [1] W. Gerstner, R. Ritz, J. L. V. Hemmen, *Biological Cybernetics* **1993**, *69*, 5 503.
- [2] H. Markram, J. Lübke, M. Frotscher, B. Sakmann, *Science* **1997**, *275*, 5297 213.
- [3] G. Q. Bi, M. M. Poo, *The Journal of Neuroscience* **1998**, *18*, 24 10464.
- [4] G. Q. Bi, M. M. Poo, *Annual Review of Neuroscience* **2001**, *24* 139.
- [5] L. I. Zhang, H. W. Tao, C. E. Holt, W. A. Harris, M. M. Poo, *Annual Review of Neuroscience* **1998**, *395* 37.
- [6] D. E. Feldman, *Neuron* **2000**, *27*, 1 45.
- [7] Y. Mu, M. M. Poo, *Neuron* **2006**, *50*, 1 115.
- [8] S. Cassenaer, G. Laurent, *Nature* **2007**, *448* 709.
- [9] V. Jacob, D. J. Brasier, I. Erchova, D. Feldman, D. E. Shulz, *The Journal of Neuroscience* **2007**, *27*, 6 1271.
- [10] D. O. Hebb, In *Wiley*. New York, **1949** .
- [11] S. Balatti, S. Ambrogio, D. C. Gilmer, D. Ielmini, *IEEE Electron Device Letters* **2013**, *34*, 7 861.
- [12] B. Chen, Y. Lu, B. Gao, Y. H. Fu, F. F. Zhang, P. Huang, Y. S. Chen, L. F. Liu, X. Y. Liu, J. F. Kang, Y. Y. Wang, Z. Fang, H. Y. Yu, X. Li, X. P. Wang, N. Singh, G. Q. Lo, D. L. Kwong, In *2011 International Electron Devices Meeting*. Washington, DC, USA, **2011** .
- [13] W. Guan, S. Long, Q. Liu, M. Liu, W. Wang, *IEEE Electron Device Letters* **2008**, *29*, 5 434.
- [14] C. Chen, S. Gao, G. Tang, C. Song, F. Zeng, F. Pan, *IEEE Electron Device Letters* **2012**, *33*, 12 1711.
- [15] C. Schindler, S. C. P. Thermadam, R. Waser, M. N. Kozicki, *IEEE Transactions on Electron Devices* **2007**, *54*, 10 2762.

- [16] R. Takemura, T. Kawahara, K. Miura, H. Yamamoto, J. Hayakawa, N. Matsuzaki, K. Ono, M. Yamanouchi, K. Ito, H. Takahashi, S. Ikeda, H. Hasegawa, H. Matsuoka, H. Ohno, *IEEE Journal of Solid-State Circuits* **2010**, *45*, 4 869.
- [17] G. Panagopoulos, C. Augustine, K. Roy, In *69th Device Research Conference*. Barbara, CA, USA, **2011** .
- [18] S. Yuasa, T. Nagahama, A. Fukushima, Y. Suzuki, K. Ando, *Nature Materials* **2004**, *3* 868.
- [19] S. H. Hong, H. Lee, *Japanese Journal of Applied Physics* **2008**, *47*, 5R 3372.
- [20] S. Shin, K. M. Kim, J. Song, H. K. Kim, D. J. Choi, H. H. Cho, *IEEE Transactions on Electron Devices* **2011**, *58*, 3 782.
- [21] A. Pirovano, A. Redaelli, F. Pellizzer, F. Ottogali, M. Tosi, D. Ielmini, A. L. Lacaita, R. Bez, *IEEE Transactions on Device and Materials Reliability* **2004**, *4*, 3 422.
- [22] G. Navarro, M. Coué, A. Kiouseloglou, P. Noé, F. Fillot, V. Delaye, A. Persico, A. Roule, M. Bernard, C. Sabbione, D. Blachier, V. Sousa, L. Perniola, S. Maitrejean, A. Cabrini, G. Torelli, P. Zuliani, R. Annunziata, E. Palumbo, M. Borghi, G. Reimbold, B. De Salvo, In *2013 IEEE International Electron Devices Meeting*. Washington, DC, USA, **2013** .
- [23] N. Ciocchini, E. Palumbo, M. Borghi, P. Zuliani, R. Annunziata, D. Ielmini, In *2013 IEEE International Electron Devices Meeting*. Washington, DC, USA, **2013** .
- [24] H. Lv, X. Xu, H. Liu, Q. Luo, Q. Liu, S. Long, M. Liu, In *2015 IEEE International Conference on Electron Devices and Solid-State Circuits (EDSSC)*. Singapore, **2015** .
- [25] T. Tsuruoka, K. Terabe, T. Hasegawa, M. Aono, *Nanotechnology* **2010**, *21*, 42 425205.
- [26] X. Zhao, S. Liu, J. Niu, L. Liao, Q. Liu, X. Xiao, H. Lv, S. Long, W. Banerjee, W. Li, S. Si, M. Liu, *Small* **2017**, *13*, 35 1603948.
- [27] X. Zhao, J. Ma, X. Xiao, Q. Liu, S. Liu, D. Chen, S. Liu, J. Niu, X. Zhang, Y. Wang, R. Cao, W. Wang, Z. Di, H. Lv, S. Long, M. Liu, *Advanced Materials* **2018**, *30*, 14 1705193.
- [28] J. Okuno, T. Kunihiro, M. Konishi, K. Materano, T. Ali, K. Kuehnel, K. Seidel, T. Mikolajick, U. Schroeder, M. Tsukamoto, T. Umebayashi, *IEEE Journal of the Electron Devices Society* **2021**, *10* 29.

- [29] J. Okuno, T. Kunihiro, K. Konishi, H. Maemura, Y. Shuto, F. Sugaya, M. Materano, T. Ali, M. Lederer, K. Kuehnel, K. Seidel, U. Schroeder, T. Mikolajick, M. Tsukamoto, T. Umebayashi, In *2021 IEEE International Memory Workshop (IMW)*. Dresden, Germany, **2021** .
- [30] J. Okuno, T. Kunihiro, K. Konishi, Y. Shuto, F. Sugaya, M. Materano, T. Ali, M. Lederer, K. Kuehnel, K. Seidel, T. Mikolajick, U. Schroeder, M. Tsukamoto, T. Umebayashi, *IEEE Journal of the Electron Devices Society* **2022**, 10 778.
- [31] W. L. Warren, B. A. Tuttle, D. Dimos, G. E. Pike, H. N. Al-Shareef, R. Ramesh, J. T. Evans, J. Jr, *Japanese Journal of Applied Physics* **1996**, 35, 2S 1521.
- [32] KNOWN Self Directed Channel Memristor, https://knowm.org/downloads/Knowm_Memristors.pdf, Accessed: 2024-07-11.
- [33] F. Liu, C. H. Chang, J. Shen, B. B. Pant, *IEEE Transactions on Magnetics* **2006**, 42, 10.
- [34] A. Tazzoli, A. Gasperin, A. Paccagnella, G. Meneghesso, In *2009 31st EOS/ESD Symposium*. Anaheim, CA, USA, **2009** .
- [35] United States Patent- Electrostatic Discharge Memristive Element Switching, <https://patentimages.storage.googleapis.com/91/76/83/0c7a7a7457b9ed/US10418810.pdf>, Accessed: 2024-07-11.
- [36] Ferrofluid stabilized with oleic acid, <https://shop.plasmachem.com/oxide-nanoparticles/121-664-magnetic-fluid-fe3o4-ca7v-aqsusp-stabilized-with-oleic-acid.html#/41-volume-10ml>, Accessed: 2023-11-03.
- [37] EMG 600p series – 601P, 603P, 605P, 607P, 608P ferrofluid, <https://ferrofluid.ferrotec.com/wp-content/uploads/sites/3/emg600psds.pdf>, Accessed: 2023-11-03.
- [38] H. Abbas, A. Ali, J. Li, T. T. T. Tun, D. S. Ang, *IEEE Electron Device Letters* **2023**, 44, 2 253.
- [39] N. Yazaki, R. Motoyoshi, S. Numata, K. Ohshima, Y. Egi, F. Isaka, T. Ohno, S. Tezuka, T. Hamada, K. Furutani, *IEEE Journal of the Electron Devices Society* **2023**, 11 467.
- [40] S. Jung, H. Lee, S. Myung, H. Kim, S. K. Yoon, S. W. Kwon, Y. Ju, M. Kim, W. Yi, S. Han, B. Kwon, B. Seo, B. Seo, K. Lee, G. H. Koh, K. Lee, Y. Song, C. Choi, D. Ham, *Nature* **2022**, 601 211.
- [41] X. Wu, A. I. Khan, H. Lee, C. F. Hsu, H. Zhang, H. Yu, N. Roy, A. V. Davydov, I. Takeuchi, X. Bao, H. S. P. Wong, E. Pop, *Nature Communications* **2024**, 15, 13.

- [42] S. D'Agostino, F. Moro, T. Torchet, Y. Demirağ, L. Grenouillet, N. Castellani, G. Indiveri, E. Vianello, M. Payvand, *Nature Communications* **2024**, *15*, 3446.
- [43] A. F. Vincent, J. Larroque, N. Locatelli, N. B. Romdhane, O. Bichler, C. Gamrat, W. S. Zhao, J. O. Klein, S. G. Retailleau, D. Querlioz, *IEEE Transactions on Biomedical Circuits and Systems* **2015**, *9*, 2 166.
- [44] M. L. Gallo, T. Tuma, F. Zipoli, A. Sebastian, E. Eleftheriou, In *2016 46th European Solid-State Device Research Conference (ESSDERC)*. Lausanne, Switzerland, **2016** .
- [45] S. Yu, X. Guan, H. S. P. Wong, In *2011 International Electron Devices Meeting*. Washington DC, USA, **2012** .
- [46] C. Merkel, D. Kudithipudi, M. Suri, B. Wysocki, *ACM Journal on Emerging Technologies in Computing Systems* **2012**, *13*, 3 1.
- [47] C. Mohan, L. A. Camuñas-Mesa, J. M. de la Rosa, E. Vianello, T. Serrano-Gotarredona, B. Linares-Barranco, *IEEE Access* **2021**, *9* 38043.
- [48] R. Xu, H. Jang, M. H. Lee, D. Amanov, Y. Cho, H. Kim, S. Park, H. Shin, D. Ham, *Nano Lett.* **2019**, *19*, 4 2411.
- [49] L. Benatti, T. Zanotti, P. Pavan, F. M. Puglisi, *Microelectronic Engineering* **2023**, *280*, 112062.
- [50] Y. Zhu, J. S. Liang, V. Mathayan, T. Nyberg, D. Primetzhofer, X. Shi, Z. Zhang, *ACS Appl. Mater. Interfaces* **2022**, *14*, 18 21173.
- [51] L. Bégon-Lours, M. Halter, Y. Popoff, Z. Yu, D. F. Falcone, B. J. Offrein, In *ESSCIRC 2021 - IEEE 47th European Solid State Circuits Conference (ESSCIRC)*. Grenoble, France, **2021** .
- [52] X. Zhu, Q. Wang, W. D. Lu, *Nature Communications* **2020**, *11*, 2439.
- [53] M. Escudero-López, E. Amat, A. Rubio, P. Pouyan, In *2016 Conference on Design of Circuits and Integrated Systems (DCIS)*. Granada, Spain, **2017** .
- [54] T. Fu, X. Liu, H. Gao, J. E. Ward, X. Liu, B. Yin, Z. Wang, Y. Zhuo, D. J. F. Walker, J. J. Yang, J. Chen, D. R. Lovley, J. Yao, *Nature Communications* **2020**, *11*, 1861.
- [55] I. A. Mihailovic, K. Klösel, C. Hierold, *Journal of Micromechanics and Microengineering* **2021**, *31*, 9.
- [56] C. Mohan, L. A. Camuñas-Mesa, J. M. de la Rosa, E. Vianello, T. Serrano-Gotarredona, B. Linares-Barranco, In *2021 IEEE International Symposium on Circuits and Systems (ISCAS)*. Daegu, Korea, **2021** .

- [57] D. Garbin, E. Vianello, O. Bicher, Q. Rafhay, C. Gamrat, G. Ghibaudo, B. DeSalvo, L. Perniola, *IEEE Transactions on Electron Devices* **2015**, *62*, 8 2494.
- [58] M. Hosomi, H. Yamagishi, T. Yamamoto, K. Bessho, Y. Higo, K. Yamane, H. Yamada, M. Sholi, H. Hachino, C. Fukumoto, H. Nagao, H. Kano, In *IEEE International Electron Devices Meeting*. Washington DC, USA, **2005**.
- [59] Memory Advanced Demonstrator 200 mm, <https://europractice-ic.com/technologies/asics/cea-leti/>, Accessed: 2023-08-16.
- [60] Skywater with Weebit ReRAM, <https://www.skywatertechnology.com/ip-partner-weebit-nano/>, Accessed: 2023-08-16.